MRI assessment of multiple dipolar relaxation time (T_{1D}) components in biological tissues interpreted with a generalized inhomogeneous magnetization transfer (ihMT) model.

Victor N. D. Carvalho[1-2], Andreea Hertanu[1], Axelle Grélard[3], Samira Mchinda[1], Lucas Soustelle[1], Antoine Loquet[3], Erick J. Dufourc[3], Gopal Varma[4], David C. Alsop[4], Pierre Thureau[3], Olivier M. Girard[1], and Guillaume Duhamel *[1]

[1] *Aix Marseille Univ, CNRS, CRMBM UMR 7339, Marseille, France*
[2] *Aix Marseille University, CNRS, ICR UMR 7273, Marseille, France*
[3] *CBMN UMR 5248, CNRS University of Bordeaux, Bordeaux INP, Pessac, France*
[4] *Department of Radiology, Division of MR Research, Beth Israel Deaconess Medical Center, Harvard Medical School, Boston, MA, United States*

T_{1D}, the relaxation time of dipolar order, is sensitive to slow motional processes. Thus T_{1D} is a probe for membrane dynamics and organization that could be used to characterize myelin, the lipid-rich membrane of axonal fibers. A mono-component T_{1D} model associated with a modified ihMT sequence was previously proposed for in vivo evaluation of T_{1D} with MRI. However, experiments have suggested that myelinated tissues exhibit multiple T_{1D} components probably due to a heterogeneous molecular mobility. A bi-component T_{1D} model is proposed and implemented. ihMT images of ex-vivo, fixed rat spinal cord were acquired with multiple frequency alternation rate. Fits to data yielded two T_{1D}s of about 500 μs and 10 ms. The proposed model seems to further explore the complexity of myelin organization compared to the previously reported mono-component T_{1D} model.

Keywords: Dipolar relaxation time; T_{1D}; Inhomogeneous magnetization transfer; ihMT; MRI contrast; Jeener-Broekaert; Myelin; Myelin Imaging.

1 Introduction

Dipolar relaxation has recently regained attention in MRI with the discovery of a new imaging modality, inhomogeneous Magnetization Transfer (ihMT) [1], which allows isolating the contribution of dipolar order effects to magnetization transfer occurring within broad macromolecular lines [2–4]. The ihMT technique is intrinsically weighted by T_{1D}, the dipolar relaxation time, hence providing a new endogenous contrast to characterize biological tissues in vivo. Although dipolar order and associated relaxation have been studied quite extensively in chemical physics [5–8], especially in the field of liquid crystals and organic crystals, little is known about this yet unexplored relaxation mechanism in biological tissues.

Similar to T_1 and T_2 spin relaxation mechanisms, T_{1D} relaxation is driven by molecular motions and can in principle deliver quantitative information about molecular dynamics and organization, which are related to motional correlation times and activation energy [9, 10]. Yet, as compared to T_1, T_{1D} is specifically sensitive to slower motional processes occurring within a frequency range corresponding to the magnitude of the local dipolar field ω_d, and on the order of 1-20 kHz depending on the motional averaging of the dipolar

*Corresponding author: G. Duhamel. Aix Marseille Univ, CNRS, CRMBM UMR 7339, 27 bd Jean Moulin, 13385 Marseille, France. guillaume.duhamel@univ-amu.fr

interactions. Formally this may be expressed as an additional relaxation term involving the spectral density of molecular motions at the local field frequency $J(\omega_d)$ [7, 11, 12]. This term indicates that T_{1D} will reach a minimum for correlation times on the order of $1/\omega_d$, corresponding to motions that are most efficient to catalyze (e.g. shorten) relaxation. Of interest, T_{1D} has been shown to be sensitive to membrane collective motions [13,14] rather than intramolecular motions, which occur at much higher rate. As collective motions in a membrane could be probed to evaluate membrane fluidity and elasticity, T_{1D} measurement with MRI could potentially provide in vivo quantification of these biological features. This is an interesting application for studying myelin, a lipid-protein (70%/30% of dry matter) multi-lamellar membrane [15], since assessing myelin fluidity may yield further understanding of demyelinating diseases, such as multiple sclerosis [16].

The theoretical model of ihMT relies on the theory of weak radio frequency (RF) saturation in solids [17], which, using the concept of spin temperature [18], allows describing the macromolecular pool by a Zeeman order and a dipolar order reservoirs effectively coupled under the effect of a single-offset RF saturation. Interestingly, the use of a symmetric dual-offset RF saturation with equal power distributed on both positive and negative frequencies decouples Zeeman order from dipolar order [2, 19]. Hence, the difference between a magnetization transfer (MT) image derived from a single offset RF saturation and a MT image derived from a dual-offset RF saturation, defined as the ihMT image, isolates the dipolar order contribution to RF saturation effects [1, 2].

In practice, single-offset (S^+) and dual-offset (S^{+-}) MT images can be obtained by applying a train of shaped RF pulses repeated every dt, prior to the image acquisition. Identical ($\Delta = +f$) frequency is applied to all pulses for S^+, whereas for S^{+-}, an alternation of the frequency from $\Delta = +f$ to $\Delta = -f$ is applied every other pulse (Fig. 1a). A modification of the dual-offset saturation scheme has been proposed to provide additional sensitivity to T_{1D} relaxation [20] and the theoretical ihMT model applied to this modified ihMT sequence enabled the formulation of an analytical solution of the ihMT signal decay as function of T_{1D} and the switching time between positive and negative frequency offset pulses. Fits of this analytical solution to experimental data led to rather long T_{1D}s estimated to ∼5-10 ms in myelinated brain tissues (white and gray matter) and ∼15-20 ms in lamellar lipid systems such as hair conditioner [20, 21]. In contrast, other biological tissues or samples, such as muscle or agarose gels, have shown much shorter dipolar relaxation times (∼1-3 ms). Long T_{1D}s in myelinated tissues most likely explain the selective contrast of ihMT images for white matter [22–25] and its high specificity for myelin [26].

The above-presented framework for the dipolar order relaxation time estimation using ihMT MRI sequences relies on a single compartment for T_{1D}. However, recent investigations have suggested that there could be multiple T_{1D} components in myelinated tissues.

Prevost et al. in [21] varied the ihMTR contrast in mouse brain by increasing dt, the repetition time between two consecutive RF pulses in the ihMT preparation (approach called T_{1D} filtering). By weighting the ihMT signal towards relatively long T_{1D}, it became clear that short T_{1D} components ($T_{1D} \ll dt$) would be filtered out from the MRI signal, enhancing the specificity of ihMT for myelinated tissues. Later on, strategies to optimize the ihMTR values in human brain by alternating bursts of strong RF pulses and a long dead time, while keeping the same global irradiated power, B_{1RMS}, were proposed [27, 28]. These configurations provided a strong sensitivity enhancement and were called boosted ihMT sequences. Duhamel et al. in [26] combined boosted ihMT sequences with various T_{1D} filtering strengths and observed signal variations in brain tissue that were not consistent with the theory if a single T_{1D} component was used to describe myelinated tissues, hence suggesting the existence of multiple T_{1D} components in myelin. An alternative view of the T_{1D} distribution can be obtained with Jeener-Broekaert measurements [29], which is one of the standard NMR pulse sequences to measure T_{1D}. A rather simple lipid system made of multilamellar vesicles mimicking the lipid composition of myelin was studied by using the Jeener-Broekaert pulse sequence and the results are shown in the Appendix A. The echo time dependence of the Jeener-Broekaert echoes unambiguously shows a multi-exponential feature, hence the existence of multiple T_{1D}s in lipid membranes. Overall these

evidences led to the belief that multiple T_{1D}s were also needed for ihMT measurements in myelinated tissues.

Previous quantitative models have not considered the effect of multiple components with nonzero T_{1D} on T_{1D} estimation with ihMT. Varma et al. [2] introduced a two-component model of ihMT and MT but assumed one component had zero T_{1D}. In subsequent work [20], when modeling data with modified ihMT preparation including varied frequency switching times, only one T_{1D} component was modeled using a complicated analytic solution for the ihMT steady state. Herein the model introduced in [20] is called the mono-component T_{1D} model.

In this paper, we propose a general model framework allowing the estimation of multiple T_{1D} components from modified ihMT MRI data. The proposed model was applied with two T_{1D} components and, herein, is called bi-component T_{1D} model. Instead of relying on an analytical solution, a fast matrix formalism was used in order to obtain a closed-form solution of the ihMT signal with minimal approximations. The mono- and bi-component T_{1D} models were compared with regard to fit results and validity of fits over different RF power regimes for experimental data measured with the modified ihMT sequence in ex-vivo rat spinal cord.

2 Theory

2.1 Dipolar order effects on magnetization transfer MRI

The biophysical model associated with the theory of ihMT with the mono-component T_{1D} is illustrated on Figure 2a, and, following the theory of weak RF saturation in solids developed by Provotorov [17], separates the macromolecular pool of protons into a Zeeman order (α) and a dipolar order (β) reservoirs, effectively coupled under the effect of off-resonance RF saturation. Using a thermodynamic interpretation of Provotorov theory [18], one can use a system of coupled differential equations to describe the evolution of the spin temperatures of the Zeeman and dipolar reservoirs:

$$\frac{d\alpha}{dt} = -R_{RFB}\,(\alpha - \beta) - R_{1B}\,(\alpha - \alpha_L)$$

$$\frac{d\beta}{dt} = R_{RFB}\left(\frac{2\pi\Delta}{D}\right)^2(\alpha - \beta) - \frac{1}{T_{1D}}\,(\beta - \beta_L)$$

in which α and β are proportional to the inverse of the Zeeman and dipolar spin temperatures respectively. $\alpha = \frac{M_{ZB}}{2\pi\Delta}$ corresponds to the net magnetization of the macromolecular pool initially equal to $\alpha_L = \frac{M_{0B}}{2\pi\Delta}$. $\beta_L \ll \alpha_L$ can be neglected. R_{RFB} is the RF saturation rate defined by $R_{RFB} = \pi\,\omega_1^2\,g_B(2\pi\Delta)$ with ω_1 the RF power of the RF pulse and g_B the normalized absorption lineshape of the macromolecular spins. D corresponds to the local dipolar field expressed in angular frequency unit, and may be calculated from the second moment of g_B.

The magnetization exchange between the macromolecular pool and the liquid pool can be further described by the modified Bloch equations such that the equations of evolution for the total spin system, considering only the longitudinal magnetization components, are given by [30, 31]:

$$\frac{dM_{ZA}}{dt} = R_{1A}\,(M_{0A} - M_{ZA}) - RM_{0B}M_{ZA} + RM_{0A}M_{ZB} - R_{RFA}M_{ZA}$$

$$\frac{dM_{ZB}}{dt} = R_{1B}\,(M_{0B} - M_{ZB}) - RM_{0A}M_{ZB} + RM_{0B}M_{ZA} + 2\pi\Delta\,R_{RFB}\,\beta - R_{RFB}M_{ZB} \tag{1}$$

$$\frac{d\beta}{dt} = -\frac{1}{T_{1D}}\beta + R_{RFB}\frac{2\pi\Delta}{D^2}M_{ZB} - R_{RFB}\left(\frac{2\pi\Delta}{D}\right)^2\beta$$

with R_{1A}, the relaxation rate of the liquid pool $\left(R_{1A} = \frac{1}{T_{1A}}\right)$, R_{1B}, the Zeeman relaxation rate of the macromolecular pool $\left(R_{1B} = \frac{1}{T_{1B}}\right)$, R, the magnetization exchange rate between the macromolecular pool and the liquid pool and R_{RFA}, the RF saturation rate defined by $R_{RFA} = \pi\,\omega_1^2\,g_A(2\pi\Delta)$.

While single-sided off-resonance RF saturation (S^+) generates dipolar order effects acting against the saturation of the Zeeman order (eq. 1), a symmetric and simultaneous dual-sided off-resonance RF saturation with equal power applied on positive and negative frequencies (S^{+-}) effectively decouples the dipolar order from Zeeman order thereby cancelling the dipolar order contribution to the MT effects. This is mathematically verified by replacing in eq. 1 the term $2\pi\Delta\,R_{RFB} = 2\pi\Delta\,\pi\omega_1^2 g_B(2\pi\Delta)$ by $\Delta\pi^2\omega_1^2 g_B(2\pi\Delta) - \Delta\pi^2\omega_1^2 g_B(-2\pi\Delta)$, which accounts for halving the RF power between $\Delta = +f$ and $\Delta = -f$, and which equals zero assuming that the lineshape g_B is symmetric [31] $g_B(2\pi\Delta) = g_B(-2\pi\Delta)$. Thus a simple difference of the generated MT images can be computed to make the ihMT image reflecting dipolar order. Then, ihMTR is computed as:

$$ihMTR = 2\frac{S^+ - S^{+-}}{S_0}, \tag{2}$$

in which S_0 is the unsaturated image.

As mentioned in Varma et al. [2], the differential equations associated with a single T_{1D} component model (Eq. 1) can be straightforwardly extended to take into account several (as indicated by i) Zeeman orders M_{ZBi} and dipolar orders β_i accounting for multi-component T_{1D} model. The bi-component T_{1D} model proposed in this work (Figure 2b) assumes a macromolecular pool divided in a fraction f_D associated with a Zeeman order M_{ZB1} coupled to a dipolar order β_1 and a fraction $(1 - f_D)$ associated with a Zeeman order M_{ZB2} coupled to a dipolar order β_2. Each dipolar order is characterized by its own relaxation time (T_{1D1} and T_{1D2}). Identical relaxation rate, R_{1B}, and lineshape, g_B, are assumed for both components. Finally, the two fractions of macromolecular pool were assumed to exchange with the same rate R with the liquid pool.

2.2 Assessing T_{1D} with ihMT

The typical ihMT experiment (Fig. 1a) was modified by Varma et al. [20] to enable T_{1D} measurements (Fig. 1b): the switching time between frequency alternation, Δt, is increased in a way that multiple pulses are applied with the same frequency before switching to the opposite frequency in the dual-offset saturation scheme. By keeping all other sequence parameters (including duty cycle and pulse bandwidth) constant, the modified ihMT signal decays as Δt increases and as a function of the value of T_{1D}.

For the mono-component T_{1D} model, an analytical solution of equation 1 was found considering the modified ihMT sequence and assuming the steady state condition (eq. 2 and appendix in [20]). This approach allowed for estimation of T_{1D} from ihMT experimental data using conventional least square optimization procedures.

To calculate the solution for the bi-component T_{1D} model, we used a matrix representation [32, 33] of equations 4 of Varma et al. [2] to describe the magnetization of each reservoir:

$$\dot{M} = AM + B \tag{3}$$

in which:

$$M = \begin{bmatrix} M_{ZA} \\ M_{ZB1} \\ \beta_1 \\ M_{ZB2} \\ \beta_2 \end{bmatrix}$$

$$A = \begin{bmatrix} -\left(R_{1A} + RM_{0B} + R_{RFA}\right) & R\,M_{0A} & 0 & R\,M_{0A} & 0 \\ R\,f_D\,M_{0B} & -\left(R_{1B} + RM_{0A} + R_{RFB}\right) & R_{RFB}\,2\pi\Delta & 0 & 0 \\ 0 & R_{RFB}\,\frac{2\pi\Delta}{D^2} & -\left[\frac{1}{T_{1D1}} + R_{RFB}\left(\frac{2\pi\Delta}{D}\right)^2\right] & 0 & 0 \\ R\left(1-f_D\right)M_{0B} & 0 & 0 & -\left(R_{1B} + RM_{0A} + R_{RFB}\right) & R_{RFB}\,2\pi\Delta \\ 0 & 0 & 0 & R_{RFB}\,\frac{2\pi\Delta}{D^2} & -\left[\frac{1}{T_{1D2}} + R_{RFB}\left(\frac{2\pi\Delta}{D}\right)^2\right] \end{bmatrix}$$

and

$$B = \begin{bmatrix} R_{1A}\,M_{0A} \\ R_{1B}\,f_D\,M_{0B} \\ 0 \\ R_{1B}\left(1-f_D\right)M_{0B} \\ 0 \end{bmatrix}.$$

Considering an event of duration t_1 in the modified ihMT sequence (i.e. a RF pulse or a relaxation delay) and assuming that A and B are constant during that period of time, a general matrix exponential solution for eq. 3 can be given by equation (6) in [34].

$$M_{t_1} = e^{At_1} M_{t=0} + A^{-1}\left(e^{At_1} - I\right) B$$

The usual power equivalent approximation for rectangular pulses [34,35] was applied to the used shaped RF pulses to make ω_1 time independent.

Thus, defining $P = e^{At_1}$ and $Q = A^{-1}\left(e^{At_1} - I\right) B$, one can rewrite:

$$M_{t_1} = PM_{t=0} + Q$$

For simplicity, t can be dropped in M_{t_1} and therefore: $M_1 = PM_{t=0} + Q$. The matrices P and Q transform $M_{t=0}$ into M_1.

Now let us consider a series of events, such as in the case of a train of pulses during the modified ihMT sequence. Consider an initial magnetization $M_{t=0}$. Applying a rectangular pulse or a delay can be described by matrices P_1 and Q_1 such that $M_1 = P_1 M_{t=0} + Q_1$. Then the successive events are described by the following equations:

$$\begin{aligned} t = t_0 \qquad & M_{t=0} \\ t = t_1 \qquad & M_1 = P_1 M_{t=0} + Q_1 \\ t = t_2 \qquad & M_2 = P_2 M_1 + Q_2 = P_2 P_1 M_{t=0} + P_2 Q_1 + Q_2 \end{aligned}$$

$t = t_3 \qquad M_3 = P_3 M_2 + Q_3 = P_3 P_2 P_1 M_{t=0} + P_3 P_2 Q_1 + P_3 Q_2 + Q_3$

$t = t_4 \qquad M_4 = P_4 M_3 + Q_4 = P_4 P_3 P_2 P_1 M_{t=0} + P_4 P_3 P_2 Q_1 + P_4 P_3 Q_2 + P_4 Q_3 + Q_4$

...

$t = t_N \qquad M_N = P_N M_{N-1} + Q_N = P_N^{eq} M_{t=0} + Q_N^{eq},$

in which P_N^{eq} and Q_N^{eq} are the equivalent matrices of applying all the N events:

$$P_N^{eq} = \prod_{i=1}^{N} P_i$$

$$Q_N^{eq} = \sum_{j=1}^{N} \left[\left(\prod_{\substack{i=j+1 \\ j<N}}^{N} P_i \right) Q_j \right]$$

in which $\prod$ is the leftwise product operator.

The steady state solution for the modified ihMT sequence is then found by imposing that $M_{t=0} = M_N$, in which N is the number of events corresponding to the periodicity of the RF saturation scheme (i.e. Δt for single offset saturation and $2\Delta t$ for dual offset saturation):

$$M_{SS} = (I - P_N^{eq})^{-1} Q_N^{eq}$$

The assumption of steady state is not necessary but was chosen to reduce the computation time of simulations and data fits. Define P_+, Q_+ the matrices P and Q for a RF pulse with a positive offset frequency; P_-, Q_- likewise; P_r, Q_r the matrices corresponding to a relaxation during the delay between two pulses. The magnetization in the steady state after the single saturation $S+$ is:

$$S^+ = (I - P_r\, P_+)^{-1} (P_r\, Q_+ + Q_r)$$

Likewise, the magnetization in the steady state after the dual saturation S^{+-} is (given $n \in \mathbb{N}^*$):

$$S^{+-}(\Delta t = n\, dt) = [I - (P_r\, P_-)^n (P_r P_+)^n]^{-1} \left\{ (P_r\, P_-)^n \left[\sum_{i=0}^{n-1} (P_r P_+)^i \right] (P_r Q_+ + Q_r) + \left[\sum_{i=0}^{n-1} (P_r P_-)^i \right] (P_r Q_- + Q_r) \right\}$$

Then

$$ihMTR(\Delta t) = 2 \frac{S^+ - S^{+-}(\Delta t)}{S_0}. \tag{4}$$

Therefore, ihMTR in the steady state can be simulated for each Δt value. Conversely, one can also estimate T_{1D1}, T_{1D2} and f_D (or other parameters) given ihMTR(Δt) data by using optimization algorithms such as non-linear least squares.

3 Methods

3.1 Ethics statement

Experiments were conducted on a fixed rat spinal cord and were performed following French guidelines for animal care from the French Department of Agriculture (Animal Rights Division), the directive 2010/63/EU of the European Parliament and of the Council of 22 September 2010 and approved by our institutional committee on Ethics in animal research (Comité d'Éthique de Marseille n°14, project authorization APAFIS#1747-2015062215062372v6).

3.2 MRI measurements

Ex-vivo modified ihMT measurements were performed on a Bruker Pharmascan 7T with a volume emitter coil and a 4-element array receiver cryoprobe on an excised, fixed rat spinal cord (cervical level) immersed in normal phosphate buffered saline (PBS) maintained at 40±1°C during all the experiment. Enough time was waited before the acquisition until the spinal cord presented a stable S_0 image, indicating that the temperature was approximately constant. The modified ihMT preparation (Fig. 1b) consisted of 2000 pulses of 0.5 ms with a delay of 0.3 ms between each pulse. The total saturation time was 1.6 s. The offset frequencies were 9700 Hz and -10300 Hz (that is slightly off-centered with respect to the free water resonance line to compensate for the chemical shift of the macromolecular line [36]). The switching time, Δt, was set to each of the values: 0.8; 1.6; 4; 8; 16; 20 ms. The root mean square power calculated over the total ihMT preparation, B_{1RMS} was set to each of the values 3.5; 5.8; 6.7; 8.0; 9.0 μT. The ihMT preparation was followed by a single slice single-shot RARE (rapid acquisition with relaxation enhancement) readout module with echo time 2.978 ms, effective echo time 23.80 ms, RARE factor = 71, partial Fourier acceleration = 1.8, FOV 20 mm x 20 mm, matrix size 128 x 128 voxels, slice thickness 4 mm. The number of averages for each individual MT contrast (single-offsets and dual-offsets) was 150 for each Δt and B_{1RMS} values. The acquisition time was about 20 hours for the whole dataset.

3.3 Fitting T_{1D}

T_{1D} maps of rat spinal cord were generated by voxelwise fitting of the solutions of the mono- and bi-component T_{1D} models to the ihMTR(Δt) images. Matlab (The MathWorks Inc., Natick, MA) was used, specifically the built-in function $lsqcurvefit$, a nonlinear least-squares solver. For the mono-component T_{1D} model, the analytical solution as presented in Varma et al. [20] was used to derive T_{1D} and A maps, in which A is a normalization factor and is equivalent to 0.5ihMTR($\Delta t = 0$). For the bi-component T_{1D} model, the solution derived from the matrix exponential approach (eq. 4) was used to extract T_{1D1}, T_{1D2}, f_D (and $1 - f_D$). Considering the sensitivity analyses in Varma et al. [20], which showed that ihMT is more sensitive to T_{1D} and less sensitive to other MT parameters when using the experimental framework of modified ihMT sequence, the following fixed parameter values [20] were used for both models: R = 26 s^{-1}, $RM_0^B/R_{1A} = 2.3$, $1/(R_{1A}T_{2A}) = 22$, $T_{2B} = 9.7\ \mu s$, $R_{1B} = 1\ s^{-1}$, $R_{1A} = (1.8)^{-1}\ s^{-1}$.

In order to assess the validity of the fits, Bayesian Information Criterion (BIC) and residual variance (resVar) were employed [37]. BIC is defined as [37]:

$$BIC = p\,ln(n) - 2\,ln(L),$$

in which p is the number of parameters to be fit and $ln(L)$ is the maximum log-likelihood of the estimated model. For a nonlinear fit with normally distributed errors [37]:

$$ln(L) = 0.5\left(-n\left(ln\,2\pi + 1 - ln\,n + ln\sum_{i=1}^{n} x_i^2\right)\right),$$

in which x_i are the residuals from the fit and n is the number of data points.

Such index promotes data fidelity (i.e. minimum residual sum of squares) and model parsimony (minimal number of model parameters) at the same time. In this sense, the best model is the one that minimizes BIC.

The residual variance is defined as [37]:

$$resVar = \frac{\sum_{i=1}^{n} x_i^2}{n - p}.$$

It quantifies the amount of variance that is not taken into account by the model. The residual variance was used only to compare two models, in the form of a ratio of their values (ratio bi : mono-component

T_{1D}). Assessing the residual variance ratio allows comparing different fitting models accounting for different degrees of freedom. In this case, the smaller the ratio is, the more advantageous the bi-component T_{1D} model.

Regions of interest (ROI) in the white matter (WM) and gray matter (GM) of the spinal cord were manually delineated in the ihMTR images (Fig. 3) and reported to the T_{1D}, A and T_{1D1}, T_{1D2}, f_D, $(1-f_D)$ maps. Mean and standard deviation values of T_{1D}, A and T_{1D1}, T_{1D2}, f_D, $(1-f_D)$ were then calculated in these ROIs.

4 Results

4.1 MRI measurements

A set of ihMTR images was obtained for each combination of Δt and B_{1RMS} values. Figure 3 shows the ihMTR(Δt) images acquired with $B_{1RMS} = 6.7$ μT. A strong white versus gray matter contrast is achieved with a clear delineation of the gray matter "butterfly" shape within the cord. One can clearly observe the ihMTR attenuation as Δt increases as a consequence of varying T_{1D} weighting.

4.2 Mono-component T_{1D} model fits

Figure 4a shows T_{1D} and A maps obtained by voxelwise fitting the analytical solution for the mono-component T_{1D} model to the ihMTR(Δt) data. All maps have the same field of view. Figure 4b shows bar plots of the T_{1D} and A values for white and gray matter for each B_{1RMS}. The BIC values are listed in Table 2 (Appendix B).

A values, which highly correlate with ihMTR, resulted in A maps sharper than T_{1D} maps. T_{1D} maps are noisier, with somewhat high values in the ihMTR signal-free area. Hence, both maps must be interpreted together: T_{1D} associated with low values of A should not be considered relevant.

Results presented in Figure 4 show that white matter consistently has a longer apparent T_{1D} than gray matter, leading to a relative T_{1D} contrast between the two structures defined as $(T_{1D}^{WM} - T_{1D}^{GM})/T_{1D}^{WM}$ of $\sim$0.17 at B_{1RMS}=3.5 μT and increasing up to $\sim$0.25 at B_{1RMS}=9 μT. Additionally, the estimated T_{1D} values in both WM and GM decrease with B_{1RMS} whereas the scaling factor A, proportional to ihMTR($\Delta t = 0$), greatly increases.

4.3 Bi-component T_{1D} fits

Matrix exponential solution of the bi-component T_{1D} model (Eq. 4) was used to fit voxelwise the same set of modified ihMTR(Δt) images of the spinal cord (Fig. 3). Figure 5a shows maps of T_{1D1}, T_{1D2}, f_D and $(1-f_D)$. All maps have the same field of view. Figure 5b shows the bar plots of T_{1D1}, T_{1D2}, f_D and $(1-f_D)$ values for white and gray matter for each B_{1RMS}. The BIC values obtained for the bi-component T_{1D} model are listed in Table 3 (Appendix B).

Overall, for white matter, long T_{1D} (T_{1D1}) on the order of 10 ms [9.8-11.3 ms] and short T_{1D} (T_{1D2}) on the order of 500 μs [403-555 μs] were found. Both T_{1D1} and T_{1D2} were consistently shorter in the gray matter; $T_{1D1}\sim$9ms [8.5-9.3 ms] and $T_{1D2}\sim$400 μs [354-418 μs]. The fraction of long T_{1D} components, f_D, was greater in white matter compared to gray matter (conversely, $1-f_D$ is greater in gray matter). In white matter, $(1-f_D)$ increases with B_{1RMS}, consistent with the more important contribution of short T_{1D} components as B_{1RMS} increases. Likewise, the maps of the short T_{1D} component (T_{1D2}) look less noisy as B_{1RMS} increases.

Figure 6 includes the bar graphs of BICs of each model and the residual variance ratio, for each RF power. Based on the BIC and residual variance ratio statistics, one can observe that the proposed bi-component T_{1D} model improves the fits (lower BIC values, and residual variance ratio <1), with best relative improvement for 5.8-8.0 μT. For the lowest (B_{1RMS}=3.5 μT) and the highest (B_{1RMS}=9.0 μT) saturation powers, BIC and residual variance ratio statistics indicate moderate, if no improvement with the proposed bi-component T_{1D} model.

5 Discussion

5.1 Multiple T_{1D}s in myelinated tissues

Since T_{1D} is a tissue property that should be unaffected by B_{1RMS}, the decrease of T_{1D}s derived from the mono-component T_{1D} model as B_{1RMS} increases (Fig. 4) suggest that a refinement of the tissue model is required. It is also consistent with the hypothesis that spinal cord would have different components with distinguishable T_{1D}s contributing to the ihMT signal: the mono-component T_{1D} model would actually perceive an apparent T_{1D} which depends on how much the short T_{1D} component is observed given the RF power. This hypothesis was further supported by simulations performed on synthetic data generated with the proposed bi-component T_{1D} model with short and long T_{1D}s, and then fit using the mono-component T_{1D} model (see Supplementary Material).

Multiple T_{1D}s imply that the hypothesis of a single dipolar spin temperature is not fulfilled within such spin systems, suggesting that spin diffusion or other exchange processes are not fast enough to average the macromolecular pool magnetization in a single effective pool. There are several possible explanations for the presence of multiple T_{1D}s in myelinated tissues. One is that myelin lipids could have a heterogeneous molecular mobility with several proton populations experiencing various kinds of molecular motions in terms of frequency (or correlation time) and intensity. These may correspond to different segmental motions along the phospholipid chain [38, 39]. Hence, dipolar order would relax in a multi-exponential fashion, as found with the NMR Jeener-Broekaert experiments on multilamellar vesicles of lipids (see Appendix A). Another possible explanation would simply be that each T_{1D} component actually corresponds to different molecular assembly, either arising from other chemical environments rather than fatty acid chains, or from other structures rather than myelin itself located in the same voxel.

Of importance, this work demonstrates that the framework combining the ihMT model with two T_{1D}s, a matrix exponential approach to solve ihMTR and a modified ihMT experiment is a viable MRI approach for multi-component T_{1D} mapping. It allowed estimating short T_{1D} on the order of 500 μs and long T_{1D} on the order of 10 ms in fixed spinal cord white matter. In terms of quantitative values, this result could be compared with those obtained on the synthetic membrane lipid system with NMR Jeener-Broekaert analysis (see Appendix A), which suggests the existence of several components, in the sub-millisecond range, 10 ms range and over 100 ms range. The T_{1D} values obtained in this study are also in close agreement with results obtained by Eliav et al. [39], who, by using a NMR sequence that combines double and zero quantum filters with magnetization transfer, measured a tri-exponential decay of the dipolar order in porcine spinal cord, with T_{1D} values of 0.11, 0.86 and 11.4 ms. Understanding the physico-chemical origins of these components is of great importance to interpret further in vivo ihMT data, however, this is outside the scope of the current study, and will require a stronger focus on in vitro and ex vivo NMR experiments.

Our results with the bi-component T_{1D} model suggest that the short T_{1D} component only measurably contributes to ihMT for powers $\geq$5.8 μT (Fig. 5a). Not only the T_{1D2} maps become less noisy as B_{1RMS} increases, but also the fraction associated with short T_{1D}, $(1 - f_D)$, increases, reaching up to 60% for white matter, while stable at >70% for gray matter. These findings are consistent with the condition for dipolar order to contribute to ihMT signal, given by $R_{RFB}\,T_{1D} > 0.01$ [4]. For example, assuming a Super-Lorentzian

lineshape, the R_{RFB} values at 10 kHz for 3.5, 5.8, 6.7, 8.0 and 9.0 μT are, respectively: 9.7, 26.1, 35.4, 50.5 and 63.6 s^{-1}, allowing observable T_{1D} higher than: 1.03, 0.38, 0.28, 0.20, 0.16 ms, respectively. However, one must consider that the contribution from very short T_{1D}s is attenuated by the T_{1D} filtering that occurs even with the shortest value of Δt (or dt). Due to hardware limitations, as well as the fact that the bandwidth of short pulses needs to remain relatively narrow to prevent direct saturation of the free pool, the dt used in this work was 0.8 ms, which does not allow efficient sampling of very short T_{1D} components ($T_{1D} \ll 0.8$ ms).

Comparison of residual variance ratio across fits suggests further insights into the T_{1D} components in tissue (Fig. 6). Low RF power (B_{1RMS}=3.5 μT) led to similar residuals for both models, indicating that the bi-component T_{1D} model does not perform much better than the mono-component T_{1D} model most likely because short T_{1D} components weakly contribute to the ihMT signal at such power level. Hence, this confirms that the mono-component T_{1D} model used in Varma et al. [20] to estimate T_{1D} is reasonable for the powers achievable in-vivo in humans. For the [5.8-8.0 μT] range, the small residual variance ratios (Fig. 6) and the lower BIC values for bi-component T_{1D} model indicate that the proposed bi-component model is more appropriate to fit the data. Interestingly, for 9.0 μT, larger residual variance ratios indicate reduced performance of both models in that power regime. This potentially implies that a model with a higher number of components would be required to more precisely describe the distribution of short T_{1D} in the system as B_{1RMS} is increased. Noteworthy, including a third T_{1D} component in the model is straight-forward from a mathematical point of view; but as new parameters are included in the model, the number of required experimental data points to estimate all model parameters should be higher. In addition, the SNR needed to correctly estimate them increases, as well as the computation time of the fitting. In the current work we limited our effort to the bi-component T_{1D} model for these reasons.

5.2 White matter / gray matter T_{1D} contrast

Our results showed significantly different T_{1D}s in white and gray matter, indicating sensitivity of T_{1D} for tissue composition and different myelin organizations. Swanson et al. [3] found T_{1D} of 11.1±1.8 ms in white matter and 4.06±1.20 ms in gray matter (bovine spinal cord ex-vivo at 40°C), by using a mono-exponential fit on the Jeener-Broekaert echoes considering values of τ greater than 600 μs. On the other hand, Varma et al. [20] found a reduced difference between white and gray matter: 6.0±0.5 ms for posterior white matter and 5.9±1.2 ms for posterior gray matter (human brain in-vivo; B_{1RMS}=3.5 μT and physiological temperature, see Table 3 in [20]), by using the mono-component T_{1D} model of ihMT. These three sets of results are not necessarily contradictory: they were performed in different specimen, temperature and interpreted with different models. The experiments in [20] used a relatively low B_{1RMS}, 3.5 μT, which was probably not enough to exploit the contribution of short T_{1D} components in gray matter, so the apparent T_{1D} reported by Varma et al. [20] in white and gray matter seemed about the same.

5.3 In vivo multiple T_{1D} measurement?

Good T_{1D} maps require ihMTR images with high SNR. In our studies, the SNR for B_{1RMS}=6.7 μT and Δt=0.8 ms was 277. This SNR level was reached with a slice thickness of 4.0 mm, spatial resolution of 0.156 mm/voxel and 150 repetitions per B_{1RMS} and per Δt. Besides, the number of Δts acquired must be large enough to estimate all the three parameters (T_{1D1}, T_{1D2} and f_D). In this study, good fits were obtained with six values of Δt, spanning from 0.8 to 20 ms. These constrains and requirements can be a limitation for in-vivo studies as the time needed to acquire a full set of ihMTR(Δt) data was about 20 hours. However, there is room for improvement. For instance, currently, the single saturation images, S^+ and S^- (Fig. 1), are acquired as many times as the dual saturation images, $S^{+-}(\Delta t)$ and $S^{-+}(\Delta t)$, while S^+ and S^- are the same for every Δt.

The dependence of apparent T_{1D} on power has been demonstrated in this work, and yielded important knowledge on how the ihMT signal is generated and filtered, all consistent with the dipolar order theory. Currently, clinical investigations of ihMT are typically performed at either 1.5T or 3T [40], which can deliver B_{1RMS} around $4\mu T$ and $2\mu T$, respectively. Whereas the RF power may reach higher levels during the saturation periods [27, 28], one has to keep these orders of magnitude in mind when interpreting in vivo ihMT data and associate them with putative T_{1D} values.

Furthermore, the T_{1D} values found in this work could differ from the values we could expect in vivo, because of the spinal cord fixation. Crosslinking tissue proteins with formaldehyde could alter the motional spectral densities and therefore affects T_{1D} values.

5.4 Limitations

This work demonstrates the feasibility of interpreting ihMT images with at least two non-zero T_{1D}, and provided an order of magnitude for the short and long T_{1D} values, 500 μs and 10 ms respectively. It did not intend to provide reference values of T_{1D} in spinal cord white and gray matter. This focus would require a higher number of specimens and validation of the T_{1D} values derived from ihMT. This could be obtained by the comparison of T_{1D} values measured with the Jeener-Broaekaert sequence and the modified-ihMT sequence on the same lipid systems and in the same experimental conditions.

Only two components (short and long T_{1D}) were considered in the proposed model. Assessment of a third very short T_{1D}, such as the one found by Eliav et al. [39], 0.11 ms, is limited by the experimental setup. The use of shorter RF pulses would be needed, however the direct saturation caused by short pulses should be avoided.

The fixed parameters (R, RM_0^B/R_{1A}, $1/(R_{1A}T_{2A})$, T_{2B}, T_{1B}, R_{1A}) enabled a fast, simple demonstration of the proposed model. This work did not aim to evaluate the influence of these parameters on the T_{1D} output. Furthermore, the assumption that both dipolar reservoirs have the same lineshape (thus T_{2B}) and same exchange rate R is a simplification, since we could not distinguish these values without further investigation of the origins of multiple dipolar reservoirs.

Finally, in this work we fit only the ihMTR(Δt) values, not the MT values. This approach was chosen because we were concerned about the ihMT parameters only. On the other hand, this means that the values found for f_D are only relative to the two components contributing to ihMT. Therefore, comparisons with qMT fits [35] in the literature may be avoided.

6 Conclusion

A bi-component T_{1D} model was proposed and better interpreted the behavior of ihMT signal acquired with the modified ihMT sequence under different RF saturation powers compared to the mono-component T_{1D} model. It allows measuring short and long T_{1D} (on the order of 500 μs and 10 ms, respectively) in spinal cord tissue. Although a theory that would relate T_{1D} values to biological membrane properties, such as fluidity and elasticity, is still required, this work is an important step in the demonstration that ihMT MRI could be an interesting tool for in vivo membrane characterization.

7 Acknowledgements

This project has received funding from the European Union's Horizon 2020 research and innovation programme under the Marie Skłodowska-Curie grant agreement N°713750. Also, it has been carried out with

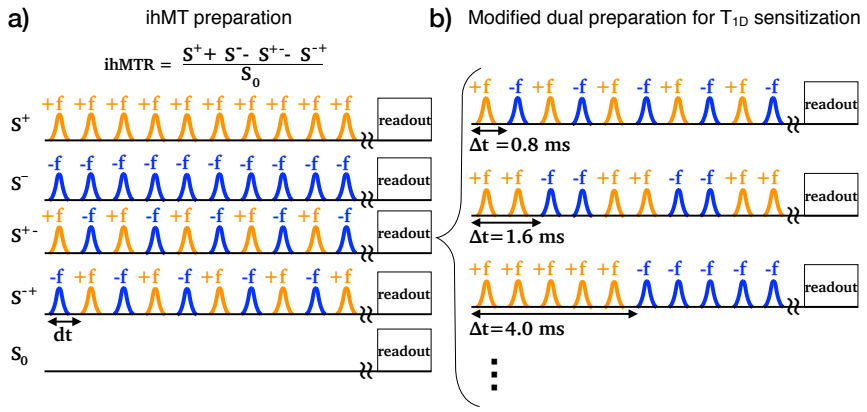


Figure 1: ihMT MRI sequence. a) ihMT preparation including single-offset and dual-symmetric offset saturations. b) Modified ihMT sequence introduced by Varma et al. [20]. In practice, the single-sided off-resonance RF saturation MT image is computed from the average of a MT image obtained with a positive offset (S^{+}) and one with a negative offset (S^{-}) in order to correct for first order asymmetry effects of g_B arising from the chemical shift of the broad macromolecular lines [36]. For signal-to-noise ratio (SNR) purpose, the dual-sided off-resonance RF saturation is also repeated twice, changing the sign of offset of the pulse (S^{+-} and S^{-+}).

the financial support of the Regional Council of Provence-Alpes-Côte d'Azur and with the financial support of the A*MIDEX (n° ANR- 11-IDEX-0001-02), funded by the Investissements d'Avenir project funded by the French Government, managed by the French National Research Agency (ANR).

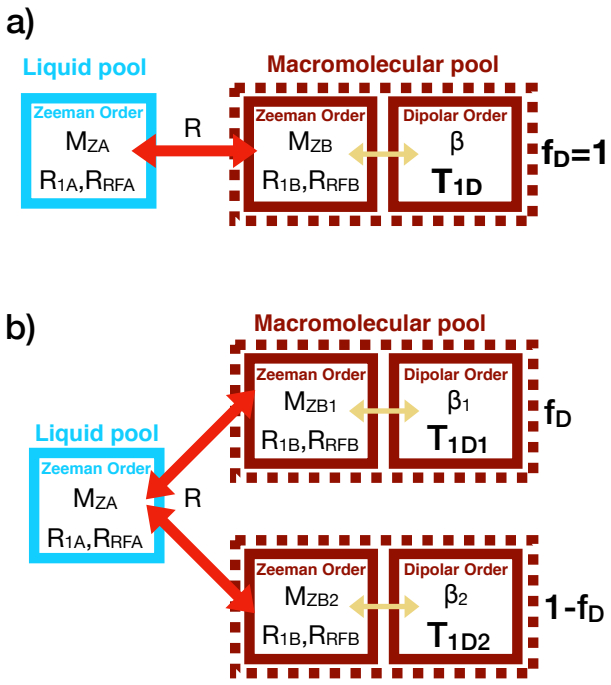


Figure 2: A) Mono-component T_{1D} ihMT model presented in [20]. B) Proposed bi-component T_{1D} ihMT model.

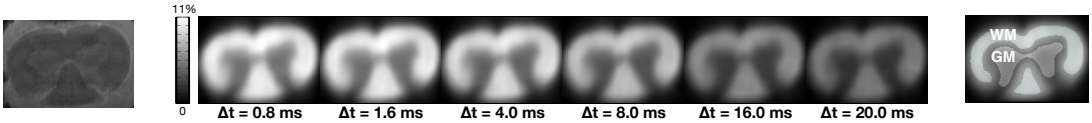


Figure 3: Representative ihMT rat spinal cord images. Left: anatomical T_2-weighted image of the rat spinal cord. Middle: ihMTR images acquired with increasing Δt (B_{1RMS}=6.7 μT). Right: Regions of interest (ROI) selected for quantitative analyses in white and gray matter.

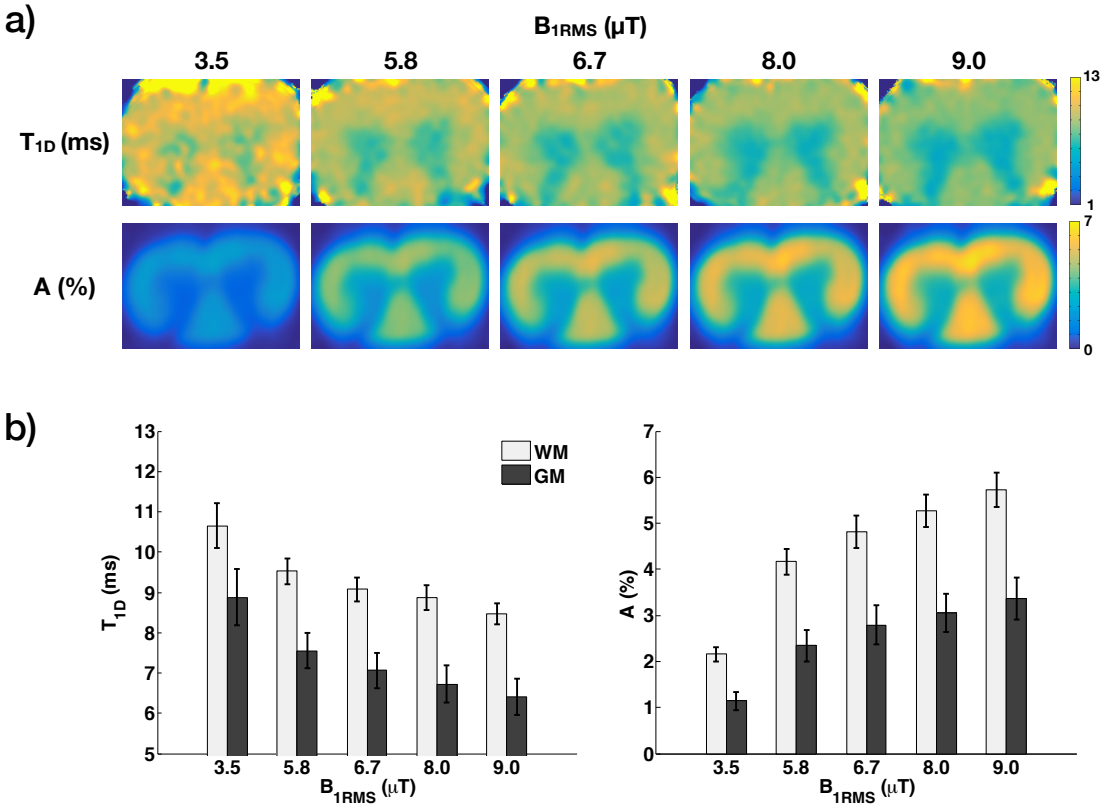


Figure 4: Mono-component T_{1D} model outcomes. a) T_{1D} (upper row) and scaling factor A (lower row) maps of rat spinal cord derived by fitting the analytical solution for the mono-component T_{1D} model [20] to ihMTR(Δt) (Fig. 3). b) Bar plots of T_{1D} (left) and A (right) values measured in ROIs selected in white (WM) and gray matter (GM) (Fig. 3) for different B_{1RMS}.

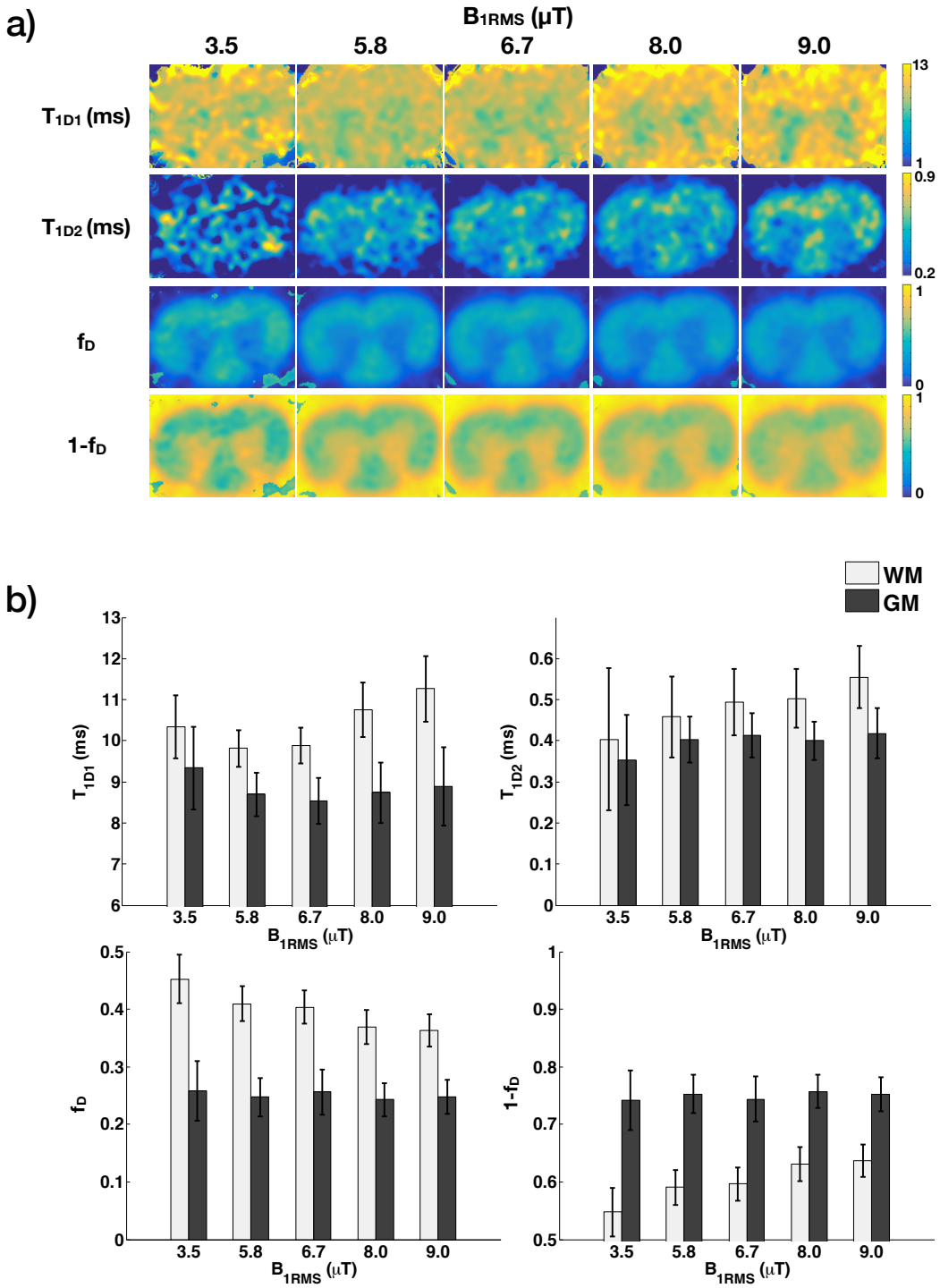


Figure 5: Bi-component T_{1D} model outcomes. a) T_{1D1}, T_{1D2}, f_D, and $(1 - f_D)$ maps of rat spinal cord obtained by using the proposed bi-component T_{1D} ihMT model. b) Bar plots of T_{1D1}, T_{1D2}, f_D and $(1 - f_D)$ values measured in ROIs selected in white (WM) and gray matter (GM) (Fig. 3) for different B_{1RMS}.

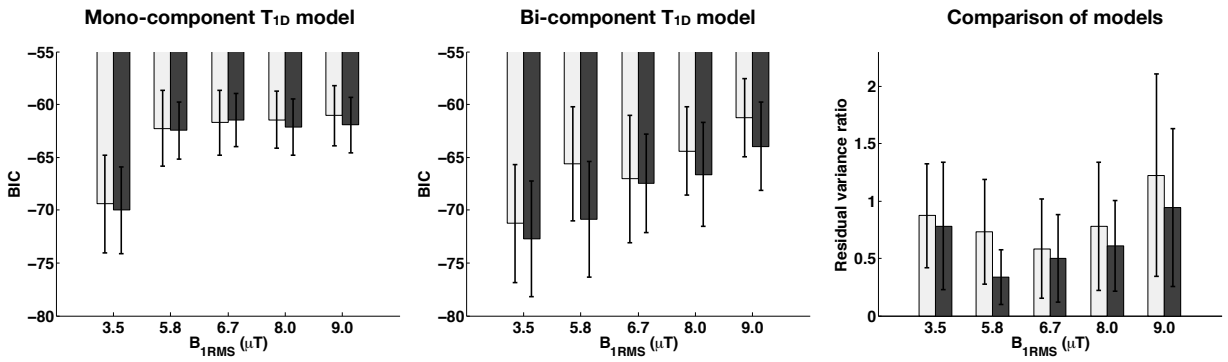


Figure 6: BIC values of each model fit: mono-component (left) and bi-component (middle). Residual variance ratio (bi : mono-component T_{1D} models) for gray and white matter for each B_{1RMS} (right). Values less than one indicate a better performance of the proposed model.

8 Appendix A: NMR Study

8.1 Synthetic membrane preparation

Lipids were purchased from Avanti Polar Lipids, Inc. (Alabaster, Alabama, USA): 1-palmitoyl-2-oleoyl-sn-glycero-3-phosphocholine (POPC), total cerebrosides (brain, porcine) and cholesterol (ovine). Multilamellar vesicles (MLV) of lipids were made by the following steps [41]:

- Appropriate amounts of lipids were weighed to obtain the proportions POPC: 40%; cholesterol 40%; cerebrosides 20% (molar ratio).
- The lipids were dissolved in organic solvent ($CHCl_3$), the solvent was evaporated, water was added, and the sample was shaken in a vortex mixer and lyophilized overnight to remove solvent traces.
- A suitable volume of heavy water, D_2O, was added to obtain a lipid hydration of 80% (v/w). Hydration is defined as the mass of water over the total mass of the system (phospholipids and water).
- The hydrated sample was then vigorously shaken in a vortex mixer, frozen in liquid nitrogen, and heated to 37°C for 10 min in a water bath. This cycle of liposome (multilamellar vesicles) formation was repeated three times until a milky dispersion was obtained at room temperature.
- The resulting dispersion was transferred into a 4-mm NMR ZrO_2 rotor (100 μl) that was placed in the magnetic field.

8.2 NMR measurements

The NMR measurements were performed on a Bruker Avance III 500 MHz spectrometer by means of a dual resonance $^1H/^{15}N$-^{31}P broad band 4mm CPMAS probe, with a Jeener-Broekaert pulse sequence [29], a standard NMR method to measure T_{1D}. This sequence consists of one 90° pulse followed by two 45° pulses: 90°(ϕ_1)-t-45°(ϕ_2)-τ-45°(ϕ_3)-acq(ϕ_4). The RF and receiver phase cycling was used as in [3] in order to eliminate multiple quantum and Zeeman order magnetization during τ. The length of the 90°-pulse was 2.62 μs, t was set to 30 μs and τ was set to 64 values from 1 μs to 10 s. The spectral width was 150 kHz and 32768 points were acquired for each τ. The number of scans was 40. Data were obtained at 312 K. The decay of the maximum absolute value of the Jeener echoes was fit with different exponential models: mono, bi, tri and quadri-exponential.

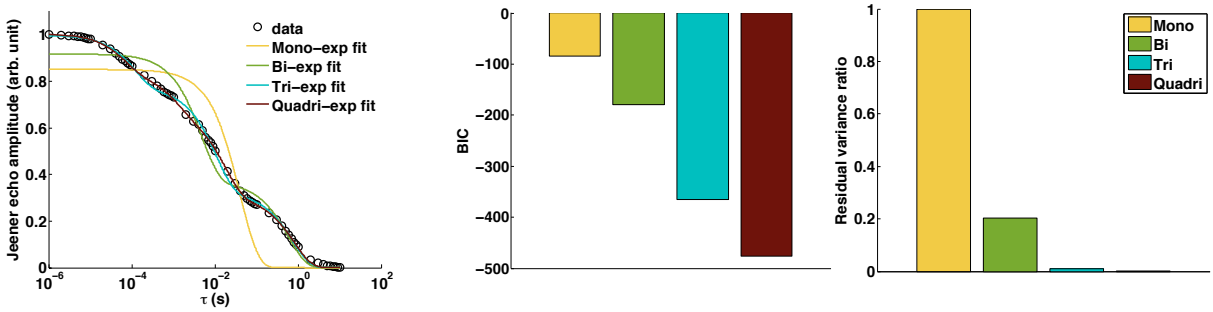


Figure 7: (left) Jeener-Broekaert echo decays in a synthetic membrane (POPC: 40%; cholesterol 40%; cerebrosides 20% (molar ratio)) and fitted with multi-exponential models. (midlle) BIC values of each exponential model fit. (right) Residual variance ratio between each exponential model and the mono-exponential model.

The decay of the Jeener echoes with τ, the delay after the second pulse, in this membrane unambiguously shows multi-exponential features. Figure 7 shows that the data points are poorly fit with a mono-exponential model, while bi-, tri-, quadri-exponential fits provide better results (lower BIC values). The T_{1D} values estimated from these fits are listed in Table 1. Although the accuracy of the quadri-exponential fit might be questionable, one can infer that a single T_{1D} is not enough to describe the dipolar relaxation in this membrane. These results suggest that the ihMT model to assess T_{1D} in complex lipid membranes such as myelin should also consider more than one dipolar component.

Model	Scaling factor	T_{1D} (ms)	BIC
Mono-exponential	0.85 ± 0.02	40.9 ± 5.9	-84.2
Bi-exponential	0.55 ± 0.02 0.37 ± 0.02	4.7 ± 0.6 577.3 ± 100.0	-179.8
Tri-exponential	0.45 ± 0.007 0.32 ± 0.006 0.23 ± 0.006	10.6 ± 0.5 721.5 ± 33.7 0.1 ± 0.01	-364.7
Quadri-exponential	0.37 ± 0.006 0.31 ± 0.003 0.16 ± 0.007 0.16 ± 0.007	17.4 ± 0.7 787.7 ± 17.5 1.2 ± 0.1 0.07 ± 0.005	-475.5

Table 1: Outcomes of multi-exponential Jeener-Broekaert echo fits obtained on a synthetic membrane (POPC: 40%; cholesterol 40%; cerebrosides 20% (molar ratio)).

9 Appendix B: Tables of fits

Table 2 lists the quantitative mean values of T_{1D}, the scaling factor, A, and the BIC values in white and gray matter, for the fits using the mono-component model. Table 3 lists all the fit results using the proposed bi-component model, as well as the BIC scores in white and gray matter, for each B_{1RMS}.

B_{1RMS} (μT)	T_{1D} (ms)	A (scaling factor) (%)	BIC
3.5	10.7 ± 0.6 (WM) 8.9 ± 0.7 (GM)	2.2 ± 0.2 (WM) 1.1 ± 0.2 (GM)	-69.4 ± 4.6 (WM) -70.0 ± 4.1 (GM)
5.8	9.5 ± 0.3 (WM) 7.6 ± 0.4 (GM)	4.2 ± 0.3 (WM) 2.3 ± 0.3 (GM)	-62.3 ± 3.6 (WM) -62.5 ± 2.7 (GM)
6.7	9.1 ± 0.3 (WM) 7.1 ± 0.4 (GM)	4.8 ± 0.4 (WM) 2.8 ± 0.4 (GM)	-61.7 ± 3.1 (WM) -61.5 ± 2.5 (GM)
8.0	8.9 ± 0.3 (WM) 6.7 ± 0.5 (GM)	5.3 ± 0.4 (WM) 3.1 ± 0.4 (GM)	-61.4 ± 2.7 (WM) -62.1 ± 2.7 (GM)
9.0	8.5 ± 0.3 (WM) 6.4 ± 0.5 (GM)	5.7 ± 0.4 (WM) 3.4 ± 0.5 (GM)	-61.1 ± 2.9 (WM) -61.9 ± 2.6 (GM)

Table 2: Mean and standard deviation values of T_{1D} and A values, as well as BIC values, in rat spinal cord white (WM) and gray matter (GM), obtained by fitting of the analytical solution for the mono-component T_{1D} model to experimental ihMTR(Δt) data for different B_{1RMS}.

B_{1RMS} (μT)	T_{1D1} (ms)	T_{1D2} (μs)	f_D	1-f_D	BIC
3.5	10.3 ± 0.8 (WM) 9.3 ± 1.0 (GM)	403 ± 173 (WM) 354 ± 110 (GM)	0.5 ± 0.04 (WM) 0.3 ± 0.05 (GM)	0.5 ± 0.04 (WM) 0.7 ± 0.05 (GM)	-71.3 ± 5.6 (WM) -72.7 ± 5.5 (GM)
5.8	9.8 ± 0.4 (WM) 8.7 ± 0.5 (GM)	458 ± 98 (WM) 403 ± 57 (GM)	0.4 ± 0.03 (WM) 0.2 ± 0.03 (GM)	0.6 ± 0.03 (WM) 0.8 ± 0.03 (GM)	-65.6 ± 5.4 (WM) -70.9 ± 5.5 (GM)
6.7	9.9 ± 0.4 (WM) 8.5 ± 0.6 (GM)	494 ± 81 (WM) 412 ± 54 (GM)	0.4 ± 0.03 (WM) 0.3 ± 0.04 (GM)	0.6 ± 0.03 (WM) 0.7 ± 0.04 (GM)	-67.0 ± 6.0 (WM) -67.4 ± 4.7 (GM)
8.0	10.8 ± 0.7 (WM) 8.7 ± 0.7 (GM)	503 ± 71 (WM) 400 ± 47 (GM)	0.4 ± 0.03 (WM) 0.2 ± 0.03 (GM)	0.6 ± 0.03 (WM) 0.8 ± 0.03 (GM)	-64.4 ± 4.2 (WM) -66.6 ± 4.9 (GM)
9.0	11.3 ± 0.8 (WM) 8.9 ± 1.0 (GM)	555 ± 76 (WM) 418 ± 61 (GM)	0.4 ± 0.03 (WM) 0.2 ± 0.03 (GM)	0.6 ± 0.03 (WM) 0.8 ± 0.03 (GM)	-61.2 ± 3.7 (WM) -64.0 ± 4.2 (GM)

Table 3: Mean and standard deviation values of T_{1D1}, T_{1D2}, f_D and $1 - f_D$, as well as BIC values, for different B_{1RMS}, in rat spinal cord white (WM) and gray matter (GM), obtained by using the proposed model.

References

[1] G. Varma, G. Duhamel, C. de Bazelaire, and D. C. Alsop. Magnetization transfer from inhomogeneously broadened lines: A potential marker for myelin. *Magn. Reson. Med.*, 73:614–622, 2015. doi:10.1002/mrm.25174.

[2] G. Varma, O.M. Girard, V.H. Prevost, A.K. Grant, G. Duhamel, and D.C. Alsop. Interpretation of magnetization transfer from inhomogeneously broadened lines (ihMT) in tissues as a dipolar order effect within motion restricted molecules. *Journal of Magnetic Resonance*, 260:67–76, 2015. https://doi.org/10.1016/j.jmr.2015.08.024.

[3] S. D. Swanson, D. I. Malyarenko, M. L. Fabiilli, R. C. Welsh, J. Nielsen, and A. Srinivasan. Molecular, dynamic, and structural origin of inhomogeneous magnetization transfer in lipid membranes. *Magn. Reson. Med.*, 77:1318–1328, 2016. doi:10.1002/mrm.26210.

[4] A. P. Manning, K. L. Chang, A. L. MacKay, and C. A. Michal. The physical mechanism of "inhomogeneous" magnetization transfer MRI. *Journal of Magnetic Resonance*, 274:125–136, 2017. http://dx.doi.org/10.1016/j.jmr.2016.11.013.

[5] Ronald Y. Dong. Relaxation and the dynamics of molecules in the liquid crystalline phases. *Progress in Nuclear Magnetic Resonance Spectroscopy*, 41(1):115 – 151, 2002.

[6] R. C. Zamar, E. Anoardo, O. Mensio, D. J. Pusiol, S. Becker, and F. Noack. Order fluctuations of the director in nematic thermotropic liquid crystals studied by nuclear magnetic resonance dipolar relaxation. *The Journal of Chemical Physics*, 109(3):1120–1124, 1998.

[7] Takahiro Ueda, Sadamu Takeda, Nobuo Nakamura, and Hideaki Chihara. Molecular motion and phase changes in long chain solid normal alkanes as studied by 1H and 13C NMR. *Bulletin of the Chemical Society of Japan*, 64(4):1299–1304, 1991.

[8] Lucia Calucci and Claudia Forte. Proton longitudinal relaxation coupling in dynamically heterogeneous soft systems. *Progress in Nuclear Magnetic Resonance Spectroscopy*, 55(4):296–323, 2009.

[9] E.J. Dufourc, C. Mayer, J. Stohrer, G. Althoff, and G. Kothe. Dynamics of phosphate head groups in biomembranes. Comprehensive analysis using phosphorus-31 nuclear magnetic resonance lineshape and relaxation time measurements. *Biophysical Journal*, 61(1):42–57, 1992. https://doi.org/10.1016/S0006-3495(92)81814-3.

[10] T. R. Molugu, S. Lee, and M. F. Brown. Concepts and methods of solid-state NMR spectroscopy applied to biomembranes. *Chemical Reviews*, 117(19):12087–12132, 10 2017. doi:10.1021/acs.chemrev.6b00619.

[11] R Van Steenwinkel. The spin lattice relaxation of the nuclear dipolar energy in some organic crystals with slow molecular motions. *Zeitschrift für Naturforschung A*, 24(10):1526–1531, 1969.

[12] O Lauer, D Stehlik, and K.H Hausser. Nuclear zeeman and dipolar relaxation due to slow motion in aromatic single crystals. *Journal of Magnetic Resonance (1969)*, 6(4):524 – 532, 1972.

[13] R. Gaspar, E.R. Andrew, D.J. Bryant, and E.M. Cashell. Dipolar relaxation and slow molecular motions in solid proteins. *Chemical Physics Letters*, 86(4):327 – 330, 1982. https://doi.org/10.1016/0009-2614(82)83516-1.

[14] O. Mensio, R.C. Zamar, F. Casanova, D.J. Pusiol, and R.Y. Dong. Intramolecular character of the intrapair dipolar order relaxation in the methyl deuterated nematic para-azoxyanisole. *Chemical Physics Letters*, 356(5–6):457 – 461, 2002. http://dx.doi.org/10.1016/S0009-2614(02)00347-0.

[15] John S. O'Brien and E. Lois Sampson. Lipid composition of the normal human brain: gray matter, white matter, and myelin. *Journal of Lipid Research*, 6(4):537–544, 1965.

[16] B. Ohler, K. Graf, R. Bragg, T. Lemons, R. Coe, C. Genain, J. Israelachvili, and C. Husted. Role of lipid interactions in autoimmune demyelination. *Biochimica et Biophysica Acta (BBA) - Molecular Basis of Disease*, 1688:10 – 17, 2004. https://doi.org/10.1016/j.bbadis.2003.10.001.

[17] B. N. Provotorov. Magnetic resonance saturation in crystals. *Sov. Phys. JETP*, 14(5):1126–1131, 1962.

[18] M. Goldman. *Spin temperature and nuclear magnetic resonance in solids*. International series of monographs on physics. Oxford: Clarendon Press, 1970.

[19] J.-S. Lee, A. K. Khitrin, R. R. Regatte, and A. Jerschow. Uniform saturation of a strongly coupled spin system by two-frequency irradiation. *J. Chem. Phys.*, 134, 234504, 2011. doi:10.1063/1.3600758.

[20] G. Varma, O. M. Girard, V. H. Prevost, A. K. Grant, G. Duhamel, and D. C. Alsop. In vivo measurement of a new source of contrast, the dipolar relaxation time, T_{1D}, using a modified inhomogeneous magnetization transfer (ihMT) sequence. *Magn. Reson. Med.*, 78:1362–1372, 2017. doi:10.1002/mrm.26523.

[21] V.H. Prevost, O.M. Girard, S. Mchinda, G. Varma, D.C. Alsop, and G. Duhamel. Optimization of inhomogeneous magnetization transfer (ihMT) MRI contrast for preclinical studies using dipolar relaxation time (T_{1D}) filtering. *NMR in Biomedicine*, 30(6):e3706, 2017. doi:10.1002/nbm.3706.

[22] O. M. Girard, V. H. Prevost, G. Varma, P. J. Cozzone, D. C. Alsop, and G. Duhamel. Magnetization transfer from inhomogeneously broadened lines (ihMT): Experimental optimization of saturation parameters for human brain imaging at 1.5 Tesla. *Magnetic Resonance in Medicine*, 73(6):2111–2121, 2015. doi:10.1002/mrm.25330.

[23] O.M. Girard, V. Callot, V. H. Prevost, B. Robert, M. Taso, G. Ribeiro, G. Varma, N. Rangwala, D. C. Alsop, and G. Duhamel. Magnetization transfer from inhomogeneously broadened lines (ihMT): Improved imaging strategy for spinal cord applications. *Magn. Reson. Med.*, 77:581–591, 2017. doi:10.1002/mrm.26134.

[24] Ece Ercan, Gopal Varma, Burkhard Mädler, Ivan E. Dimitrov, Marco C. Pinho, Yin Xi, Benjamin C. Wagner, Elizabeth M. Davenport, Joseph A. Maldjian, David C. Alsop, Robert E. Lenkinski, and Elena Vinogradov. Microstructural correlates of 3D steady-state inhomogeneous magnetization transfer (ihMT) in the human brain white matter assessed by myelin water imaging and diffusion tensor imaging. *Magnetic Resonance in Medicine*, 80(6):2402–2414, 2018.

[25] Bryce L. Geeraert, R. Marc Lebel, Alyssa C. Mah, Sean C. Deoni, David C. Alsop, Gopal Varma, and Catherine Lebel. A comparison of inhomogeneous magnetization transfer, myelin volume fraction, and diffusion tensor imaging measures in healthy children. *NeuroImage*, 182:343 – 350, 2018. Microstructural Imaging.

[26] G. Duhamel, V.H. Prevost, M. Cayre, A. Hertanu, S. Mchinda, V.N. Carvalho, G. Varma, P. Durbec, D.C. Alsop, and O.M. Girard. Validating the sensitivity of inhomogeneous magnetization transfer (ihMT) MRI to myelin with fluorescence microscopy. *NeuroImage*, 199:289 – 303, 2019.

[27] S. Mchinda, G. Varma, V. H. Prevost, A. Le Troter, S. Rapacchi, M. Guye, J. Pelletier, J. Ranjeva, D. C. Alsop, G. Duhamel, and O. M. Girard. Whole brain inhomogeneous magnetization transfer (ihMT) imaging: Sensitivity enhancement within a steady-state gradient echo sequence. *Magn. Reson. Med.*, 79:2607–2619, 2018. doi:10.1002/mrm.26907.

[28] G. Varma, O.M. Girard, S. Mchinda, V.H. Prevost, A.K. Grant, G. Duhamel, and D.C. Alsop. Low duty-cycle pulsed irradiation reduces magnetization transfer and increases the inhomogeneous magnetization transfer effect. *Journal of Magnetic Resonance*, 296:60 – 71, 2018.

[29] J. Jeener and P. Broekaert. Nuclear magnetic resonance in solids: Thermodynamic effects of a pair of RF pulses. *Phys. Rev.*, 157:232–240, May 1967. doi:10.1103/PhysRev.157.232.

[30] H.N. Yeung, R.S. Adler, and S.D. Swanson. Transient decay of longitudinal magnetization in heterogeneous spin systems under selective saturation. IV. Reformulation of the spin-bath-model equations by the Redfield-Provotorov theory. *Journal of Magnetic Resonance, Series A*, 106(1):37 – 45, 1994.

[31] C. Morrison, G. Stanisz, and R.M. Henkelman. Modeling magnetization transfer for biological-like systems using a semi-solid pool with a super-lorentzian lineshape and dipolar reservoir. *Journal of Magnetic Resonance, Series B*, 108(2):103–113, 1995. https://doi.org/10.1006/jmrb.1995.1111.

[32] Victor N. D. Carvalho, Olivier M. Girard, Andreea Hertanu, Samira Mchinda, Lucas Soustelle, Axelle Grélard, Antoine Loquet, Erick J. Dufourc, Gopal Varma, David C. Alsop, Pierre Thureau, and Guillaume Duhamel. Assessment of two T1D components within myelinated tissue with ihMT MRI. *In Proceedings of the 27th Annual Meeting of ISMRM*, Montreal, Canada, 2019. Abstract 4915.

[33] Andreea Hertanu, Olivier M. Girard, Victor N. D. Carvalho, Lucas Soustelle, Gopal Varma, David C. Alsop, and Guillaume Duhamel. Toward quantitative inhomogeneous magnetization transfer (qihMT) using a general matrix exponential model. *In Proceedings of the 27th Annual Meeting of ISMRM*, Montreal, Canada, 2019. Abstract 0428.

[34] S. Portnoy and G. J. Stanisz. Modeling pulsed magnetization transfer. *Magn. Reson. Med.*, 58:144–155, 2007. doi: 10.1002/mrm.21244.

[35] John G Sled and G.Bruce Pike. Quantitative interpretation of magnetization transfer in spoiled gradient echo mri sequences. *Journal of Magnetic Resonance*, 145(1):24 – 36, 2000.

[36] Valentin H. Prevost, Olivier M. Girard, Gopal Varma, David C. Alsop, and Guillaume Duhamel. Minimizing the effects of magnetization transfer asymmetry on inhomogeneous magnetization transfer (ihMT) at ultra-high magnetic field (11.75 t). *Magnetic Resonance Materials in Physics, Biology and Medicine*, 29(4):699–709, Aug 2016.

[37] Andrej-Nikolai Spiess and Natalie Neumeyer. An evaluation of R^2 as an inadequate measure for nonlinear models in pharmacological and biochemical research: a monte carlo approach. *BMC Pharmacology*, 10(1):6, 2010.

[38] R. Bar-Adon and H. Gilboa. Molecular motions and phase transitions. NMR relaxation times studies of several lecithins. *Biophysical Journal*, 33(3):419 – 434, 1981.

[39] Uzi Eliav, Gil Navon, and Peter J. Basser. Multi-exponential decay of dipolar order in spinal cord and its correlation to spin diffusion. *In Proceedings of the 27th Annual Meeting of ISMRM*, Montreal, Canada, 2019. Abstract 2288.

[40] E. Van Obberghen, S. Mchinda, A. le Troter, V.H. Prevost, P. Viout, M. Guye, G. Varma, D.C. Alsop, J.-P. Ranjeva, J. Pelletier, O. Girard, and G. Duhamel. Evaluation of the sensitivity of inhomogeneous magnetization transfer (ihMT) MRI for multiple sclerosis. *American Journal of Neuroradiology*, 39(4):634–641, 2018.

[41] A. Grelard, A. Couvreux, C. Loudet, and E.J. Dufourc. Solution and solid state NMR of lipids. In Larijani B, Woscholski R, Rosser CA, eds. Methods in Molecular Biology: Lipid Signaling Protocols. Totowa, USA: Humana press (Springer). pages 111–133, 2009.